Magnetic order and surface state gap in $(Sb_{0.95}Cr_{0.05})_2$ Te_3

T. K. Dalui,[1] P. K. Ghose,[1] S. Majumdar,[1] S. K. Mahatha,[2] F. Diekmann,[3] K. Rossnagel,[2,3] R. Tomar,[4] S. Chakraverty,[4] A. Berlie,[5] and S. Giri[1,*]

[1]*School of Physical Sciences, Indian Association for the Cultivation of Science, Jadavpur, Kolkata 700032, India*
[2]*Ruprecht Haensel Laboratory, Deutsches Elektronen-Synchrotron DESY, D-22607 Hamburg, Germany*
[3]*Institute of Experimental and Applied Physics, Kiel University, D-24098, Germany*
[4]*Nanoscale Physics and Device Laboratory, Institute of Nano Science and Technology, Phase-10, Sector-64, Mohali, Punjab 160062, India*
[5]*ISIS Neutron and Muon Facility, Science and Technology Facilities Council, Chilton, Oxfordshire, OX11 0QX, United Kingdom*

(Received 23 September 2020; revised 10 December 2020; accepted 5 February 2021; published 22 February 2021)

Magnetic transition element doping in topological insulators, which breaks the time-reversal symmetry, gives rise to the diverse range of exotic consequences, though proper understanding of the magnetic order has rarely been attempted by using any microscopic experiments. We report the occurrence of the magnetic order in $(Sb_{0.95}Cr_{0.05})_2Te_3$ using the muon spin relaxation studies. The asymmetry curve at low temperature (T) shows an evidence of a damped oscillation, providing a clue about the internal magnetic field ($H_{\rm int}$), which follows $H_{\rm int}(T) = H_{\rm int}(0)[1 - T/T_C]^{\beta}$ with ordering temperature $T_C \approx 6.1$ K and critical exponent $\beta \approx 0.22$. The critical exponent is close to the two-dimensional XY-type interaction. The magnetization curves at low T exhibit a ferromagnetic behavior at low field (H) and the de Haas–van Alphen (dHvA) effect at high H. The analysis of the dHvA oscillation proposes the charge carrier that acts like a massive Dirac fermion. The Berry phase, as obtained from the Landau-level fan diagram, suggests a surface state gap at the Dirac point. The complex electronic structure is discussed by correlating the magnetic order attributed to the Cr doping in Sb_2Te_3.

DOI: 10.1103/PhysRevB.103.064428

I. INTRODUCTION

Magnetic topological insulator (TI) has recently attracted special attention for tremendous potentials in the next generation of the spintronic applications having low-energy consumption, dissipationless electronic devices, and quantum information processing [1–5]. Integration of magnetic order with the topological insulating state in a crystal leads to a breaking of time-reversal symmetry (TRS), which has been proposed to open a gap at the Dirac point of the topological surface state [2]. By tuning the Fermi energy level between the gap, a quantum Hall effect at zero magnetic field, i.e, quantum anomalous Hall effect (QAHE), has been realized in the magnetic TIs [3–6]. Thus, the TRS breaking in TI provokes huge fundamental interests for the exotic consequences, like narrow-gap massive Dirac fermions [2], chiral Majorana fermions [7], in addition to QAHE. The magnetic TIs have been experimentally explored by doping the 3*d* transition elements in the TIs [8–12], although exploring the nature of magnetic order has been rarely attempted microscopically in diluted TIs [10].

The binary Sb_2Te_3 crystallizes in the tetradymite structure, which has been observed for Bi_2Te_3 [13]. The Sb_2Te_3 drew special attention, when this compound was identified as a robust three-dimensional (3D) TI [14,15]. The antisite defects, where the significant fractions of Sb and Te exchange their lattice positions, are inherent to this compound, leading to a *p*-type electric conduction [16,17]. Recent studies of the 3*d* transition element doping in Sb_2Te_3 proposed the QAHE, although microscopic understanding is far from the proper comprehension [6]. The combined studies of the density functional theory and the complementary microscopic experiment proposed that the dopants not only integrated the magnetic order, but also significantly modified the electronic structures depending upon the dopant 3*d* elements. The Fe doping has been suggested to modify the band structure with the multiple Fermi pockets, in contrast to the single frequency as detected for pure Sb_2Te_3 [18]. The antiferromagnetic (AFM) exchange interaction has been suggested for Fe [19] and Co [20] doping in Sb_2Te_3. In contrast, the ferromagnetic (FM) order has been suggested for the Mn [21,22] and V [23–27] doping in Sb_2Te_3. The narrow-band-gap semiconducting properties have been realized from the infrared spectroscopy due to V and Cr doping in Sb_2Te_3 [28], suggesting a possible occurrence of QAHE [29].

The Cr doping in Sb_2Te_3 has been identified as one of the most exciting consequences. The strain-driven band-gap engineering, leading to QAHE, was suggested from the first-principles calculations in Cr-doped Sb_2Te_3 [30], which was, in fact, realized in the films, grown by the molecular-beam epitaxy [31]. The Cr doping tunes the defect-induced carrier concentration in $Sb_{2-x}Cr_xTe_3$ films [32]. The ferromagnetic order has been suggested for the $Sb_{2-x}Cr_xTe_3$ films [33–35] and crystals [36,37]. Intriguingly, the topological surface state of $Cr_{0.05}Sb_{1.95}Te_3$ was found spin polarized in the surface plane while the bulk exhibited a ferromagnetism with an out-of-plane easy axis [38]. Thus, Cr doping in Sb_2Te_3 provides a

*Corresponding author: sspsg2@iacs.res.in

fertile ground for testing fundamental aspects of the electronic and magnetic structure. Until now, the possible FM behavior at low temperature has been proposed from the bulk magnetization study for $Sb_{2-x}Cr_xTe_3$, although the nature of the magnetic order has not been verified by using any microscopic experiments.

In this paper we propose a magnetic order with an ordering temperature (T_C) of 6.1(4) K, as obtained from the muon spin relaxation (μSR) studies in $(Sb_{0.95}Cr_{0.05})_2Te_3$. The internal magnetic field $H_{\rm int}$ follows as $H_{\rm int}(T) = H_{\rm int}(0)[1 - T/T_C]^{\beta}$ with $H_{\rm int}(0) = 37.1(4)$ Oe and $\beta \approx 0.22(1)$, which is close to the theoretically calculated value (0.23) for the two-dimensional (2D) XY model [39–41]. At low field (H), the FM behavior is indicated by the nonlinear magnetization curve for both the measurements along the c axis and perpendicular to the c axis. At higher H, an apparent signature of the de Haas–van Alphen (dHvA) oscillations is evident at low T. The Berry phase is determined from the Landau-level fan diagram, which indicates the opening of a surface gap at the Dirac point. Furthermore, the charge carriers resemble as the massive Dirac fermions. The significant changes in the electronic structure have been discussed due to the 5% Cr doping in Sb_2Te_3.

II. EXPERIMENTAL DETAILS

Single crystal of $(Sb_{0.95}Sb_{0.05})_2Te_3$ was grown by the modified Bridgman method. The Sb granules (99.999%, Sigma Aldrich), Cr powder (99.99%, Sigma Aldrich), and Te powder (99.999%, Sigma Aldrich) were mixed homogeneously in a stoichiometric ratio of 1.9:0.1:3. The mixture kept in a quartz tube was sealed in a vacuum of $\sim 10^{-6}$ torr. The crystal growth involved the heating at 900 °C for 48 h, followed by a slow cooling of 3 °C/h down to 500 °C. The shiny silver colored single crystals were obtained with a maximum area of $\sim 5 \times 4$ mm^2. The grown crystals, cleaved from the smooth and shiny surfaces, were used for the measurements. The phase purity and crystal structure were checked by the powder x-ray diffraction technique by using Cu-$K\alpha$ radiation in a PANalytical X'Pert PRO diffractometer. High-resolution transmission electron microscopy (HRTEM) was performed by using a JEOL TEM 2010. Energy dispersive x-ray spectroscopy (EDS) measurement was performed in a JEOL JSM-6010LA scanning electron microscope (SEM) to confirm the composition and the homogeneity of the single crystals. X-ray photoemission spectroscopy (XPS) was recorded with a spectrometer of Omicron Nanotechnology. The electrical transport measurements were carried out by using a physical property measurement system (PPMS II, Quantum Design) by using a standard four-probe technique. The magnetic measurements were done in a Vibrating Sample Magnetometer of a PPMS, Quantum Design.

The crystals were cleaved at room temperature in ultra-high vacuum and angle-resolved photoemission spectroscopy (ARPES) measurements were performed by using a combination of SCIENTA-R4000WAL electron energy analyzer with a 2D-CCD detector and a high-flux monochromatic SPECS UVS 300 helium discharge lamp. All the photoemission experiments were performed at 70 K by using a He $I\alpha$ (21.218 eV) resonance line to excite the photoelectrons from the sample surface and at a base pressure lower than 10^{-9} mbar. The energy and angular resolution were better than 30 meV and 0.2°, respectively. Zero binding energy ($E - E_F$) was by using a Fermi edge from a polycrystalline gold foil.

The μSR studies were performed using the HIFI spectrometer at the ISIS facility, Rutherford Appleton Laboratory, UK, both in zero field. The small pieces of the crystals with thickness larger than 1.5 mm were covered on the sample holder of diameter ~50 mm. Thus, the crystallographic c axis was perpendicular to the sample holder and, therefore, the longitudinal magnetic field was applied along the c axis. The μSR experiment involves implanting an ensemble of spin-polarized positive muons into the sample that come to rest at interstitial sites. Each muon precesses in the sum of the local magnetic field from the local environment and decays into a positron and two neutrinos, with a mean lifetime (τ_μ) of 2.2 μs. If the internal field is homogeneously distributed, a coherent precession of the muon spin is expected with $\omega = \gamma_\mu H$, where H is the local magnetic field, γ_μ ($= 2\pi \times 13.55$ MHz kOe^{-1}) is the gyromagnetic ratio of the muon, and ω is the precession frequency of the muon spin. The positron is emitted preferentially in the direction of the muon spin at the time of decay. Therefore, the detection of the decay of positrons allows to determine the time evolution of the muon spin polarization. The asymmetry of the muon decay is calculated by $A(t) = [N_{\rm F}(t) - \alpha N_{\rm B}(t)]/[N_{\rm F}(t) + \alpha N_{\rm B}(t)]$, where $N_{\rm B}(t)$ and $N_{\rm F}(t)$ are the number of counts of the detectors in the forward and backward positions, and α is a constant, as determined from the calibration measurements made in the normal state with a small 20-Oe transverse applied magnetic field. The data are analyzed using the MANTID software package [42].

III. EXPERIMENTAL RESULTS AND DISCUSSIONS

The element mapping of the crystals is performed by using SEM. The compositions are found quite uniformly throughout the crystal with the ratio 1.90:0.10:3.08 for Sb:Cr:Te, respectively, which are close to the desired composition. The x-ray diffraction studies at 300 K are performed for both the crystal and powdered samples. The crystals are crushed into fine powder, which have been considered for the powder diffraction studies. Figure 1(a) depicts the powder diffraction pattern at 300 K. The continuous curve demonstrates the Rietveld refinement by using $R\bar{3}m$ space group with the refined positional coordinates Sb/Cr (0, 0, 0.3989(5)), Te1 (0, 0, 0.2100(5)), and Te2 (0,0,0). The refined lattice constants are obtained as $a = 4.2695(1)$ Å and $c = 30.4825(9)$ Å, which is consistent with the previous reports [43,44], with the reliability parameters R_w (%) = 3.13, R_{exp} (%) = 2.52, and $\chi^2 = 1.67$. The vertical lines and the curve below the diffraction pattern show the diffraction peaks and the difference plot, respectively, pointing towards a high purity of the sample without any impurity phase. Figure 1(b) depicts the diffraction pattern of the crystal with the planes parallel to the (003) plane [44].

The HRTEM image of a portion of a particle is shown in Fig. 1(c). The image confirms the undistorted plane, which exists until the edge of the particle, as shown by an arrow. The results indicate absence of the secondary phase, atom clustering, or disorder in the crystal. An example of a more

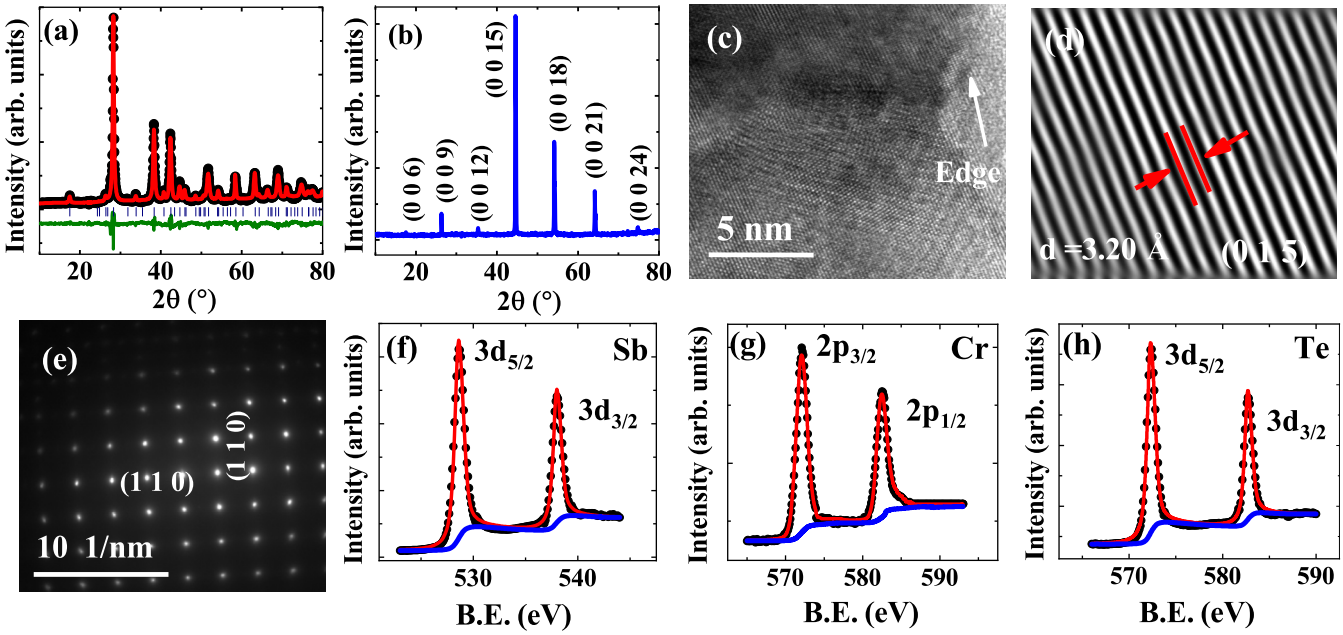

FIG. 1. (a) X-ray powder diffraction patterns (symbols) with Rietveld refinement (solid curves) of diffraction pattern and (b) diffraction pattern of the single crystal along the planes parallel to the (003) at 300 K. TEM image of (c) a portion of a particle and the planes identified as (015) in (d). The (e) SAD pattern with the assigned Miller indices. The core-level XPS of (f) Sb, (g) Cr, and (h) Te with the fitted continuous curves and backgrounds.

clear picture of a plane is further highlighted in Fig. 1(d). The spacing between the plane [$d_{(015)}$] is 3.20 Å, which matches the $d_{(015)}$ value, as obtained from the x-ray diffraction studies. Figure 1(e) shows the selected area electron diffraction (SAD) pattern with the assigned Miller indices. The periodic pattern of the spots in the SAD pattern implies the high quality of the crystal. The XPS results are shown in Figs. 1(f)–1(h), where the continuous curves show the fits. The $2p_{3/2}$ and $2p_{1/2}$ components are obtained for the Cr and the $3d_{5/2}$ and $3d_{3/2}$ contributions are obtained for the Sb and Te. The XPS is useful for determining the composition using $\rho_{Se}/\rho_{Bi} = (I_{Se}/S_{Se})/(I_{Bi}/S_{Bi})$. Here, ρ is the atomic density, I is the integrated peak intensity, as obtained from the area under the deconvoluted curve, and S the atomic sensitivity factor [45]. Considering the available values of S_{Cr}, S_{Sb}, and S_{Te} from literature [46], the values of ρ_{Cr}/ρ_{Sb}, ρ_{Cr}/ρ_{Te}, and ρ_{Sb}/ρ_{Te} are 0.0691, 0.0421, and 0.608, respectively. These values provide the ratio of Sb:Cr:Te, which is close to that observed as 1.88:0.13:3.09, respectively, as obtained from the SEM EDS.

The temperature (T) variations of resistivity are recorded in zero field and magnetic field, H parallel (∥) and perpendicular (⊥) to the crystallographic c axis. Thermal variations of the resistivity (ρ_{xx}) for selected H, ∥ to c axis are shown in Fig. 2(a), where the subscript "xx" points to the direction of current and the measured voltage in the same direction. The residual resistivity ratio, as obtained from the value of ρ_{xx} at 2 and 300 K, primarily determines the quality of the crystal. The ratio is ∼9.5, which is reasonably large, suggesting a good crystalline nature of the crystal [47,48]. The values of $\rho_{xx}(T)$ increase with H. The percentage of magnetoresistance (MR), defined as $[\rho_{xx}(H) - \rho_{xx}(0)]/\rho_{xx}(0) \times 100$, is recorded with H. The ∥ component of the MR-H curves is depicted in Fig. 2(b) at selected T. The value of MR(%) at 2.3 K is ∼178 for 90 kOe, which is comparable to the Sn doping [44]. It is, however, higher than the value of the pristine Sb_2Te_3 [43,47]. We note that the MR increases with increasing T until ∼20 K, above which it decreases with further increase in T. The MR(%) at 20 K is ∼210 for $H = 90$ kOe. The semiclassical approach of the Kohler's rule, defined as MR $\propto (H/\rho_0)^2$ [49], has been tested for the different systems such as, quasi-two-dimensional metal [50], graphite and bismuth [51], Weyl semimetal [52], topological semimetals [53]. This rule was also found to hold for the topological semimetals having two types of carriers [54]. We test the Kohler's rule

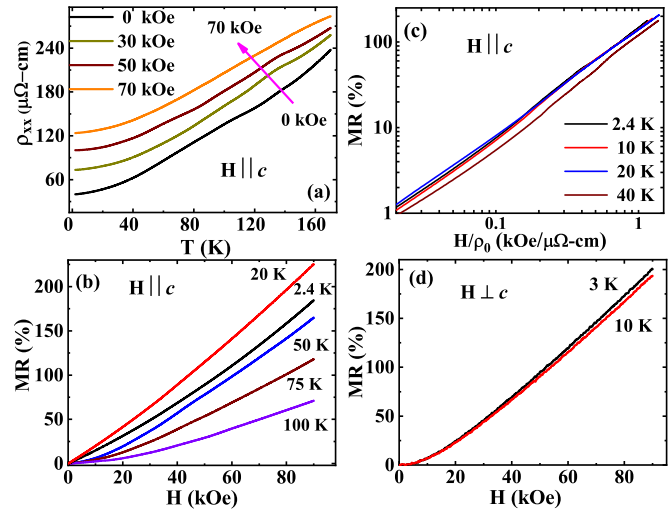

FIG. 2. The (a) ρ_{xx} with T at selected H, (b) MR(%) with H at selected T, and (c) MR(%) with scaled H/ρ_0 for different T, for the ∥ component. (d) MR(%) with H at selected T for the ⊥ component.

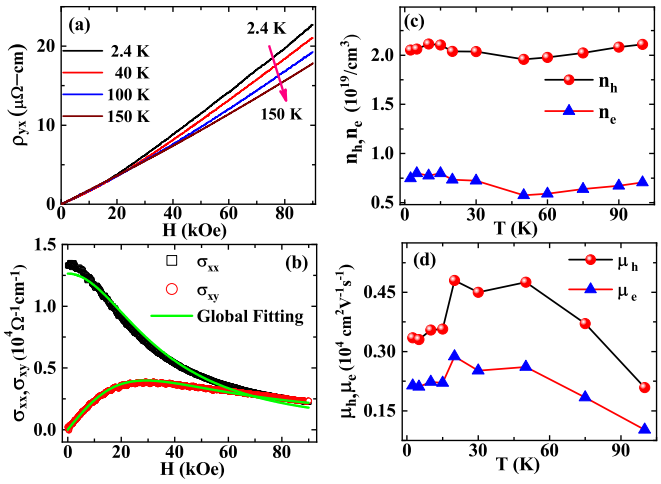

FIG. 3. (a) Hall resistivity ρ_{yx} with H at selected T. (b) Example of the global fitting of thermal variation of conductivities using Eqs. (1) and (2) at 2.4 K. The T variations of (c) n_e and n_h, and (d) μ_e and μ_h.

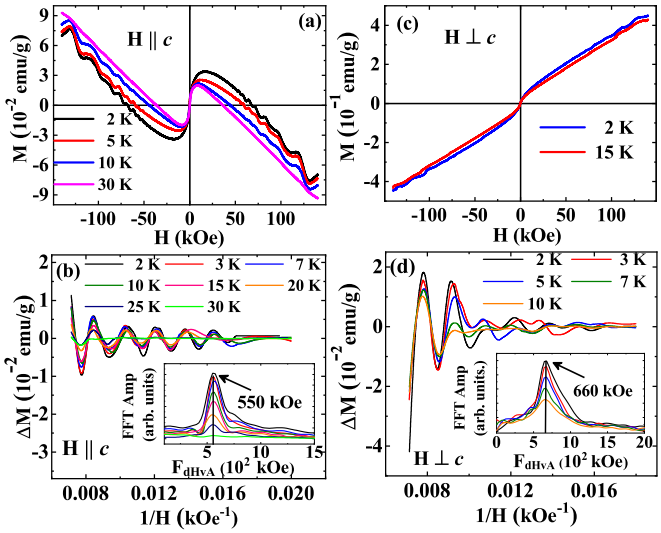

FIG. 4. Magnetic hysteresis loop at selected temperatures for the (a) ∥ and (c) ⊥ components, showing the dHvA effects. The oscillatory component (ΔM) with $1/H$ at selected T for the (b) ∥ and (d) ⊥ components. Inset depicts the amplitude of FFT component with frequency (F_{dHvA}), showing a peak around 550 and 660 kOe for the ∥ and ⊥ component, respectively.

using MR $= \alpha(H/\rho_0)^m$ with $m = 1.3$ and $\alpha = 5.3 \times 10^{-10}$ $(\Omega\,\mathrm{cm/kOe})^{1.3}$, where ρ_0 is the resistivity in zero field. Figure 2(c) illustrates the satisfactory fit of the Kohler's rule, where all the plots collapse into a single curve below 20 K. Figure 2(d) exhibits the ⊥ component of the MR-H curves at two selected T.

The resistivity is measured in the Hall geometry to probe the carrier concentration and mobility. For the Hall geometry, the ρ_{yx} is defined as $\rho_{yx} = (V_y/I_x)t$, where t is the thickness of the sample, and V_y is the transverse voltage in the presence of a magnetic field recorded along the ⊥ direction to the direction of the current I_x. To avoid the resistivity contribution from the small unavoidable mismatch in the Hall resistivity contacts, the $\rho_{yx}(H)$ is obtained considering $\rho_{yx}(H) = [\rho_{yx}(+H) + \rho_{yx}(-H)]/2$. The values of $\rho_{yx}(H)$ are depicted with H at selected T in Fig. 3(a). The nonlinear $\rho_{yx} - H$ plots primarily indicate the dominant contributions from both the electrons and holes [54,55]. The semiclassical two-band model [56] has been used to determine electron (n_e), hole (n_h) densities, electron (μ_e), and hole (μ_h) mobilities from the $\rho_{yx} - H$ curves at different T for different systems [54,55] following

$$\sigma_{xy} = \left[n_h \mu_h^2 \frac{1}{1 + (\mu_h H)^2} - n_e \mu_e^2 \frac{1}{1 + (\mu_e H)^2} \right] eH \qquad (1)$$

and

$$\sigma_{xx} = e\left[n_h \mu_h \frac{1}{1 + (\mu_h H)^2} + n_e \mu_e \frac{1}{1 + (\mu_e H)^2} \right], \qquad (2)$$

with $\sigma_{xy} = \frac{\rho_{yx}}{\rho_{yx}^2 + \rho_{xx}^2}$ and $\sigma_{xx} = \frac{\rho_{xx}}{\rho_{xx}^2 + \rho_{yx}^2}$. The global fittings of σ_{xx} and σ_{xy} are performed using Eqs. (1) and (2), which is shown in Fig. 3(b) by the continuous curve. As obtained from the reasonable fit, the values of n_e and n_h with T are depicted in Fig. 3(c). The values of n_h and n_e are $\sim 2.1 \times 10^{19}$ and $\sim 0.75 \times 10^{19}$ cm^{-3} at 2 K, respectively, pointing towards a dominant hole carrier. Temperature variations of μ_e and μ_h are depicted in Fig. 3(d). The μ_e and μ_h are strongly temperature dependent. The μ_e and μ_h increase, showing a broadened maximum in the range of ~20–45 K, above which they decrease with increasing T.

The magnetization curves are recorded at low temperature for H ∥ and ⊥ to the c axis, which are shown in Figs. 4(a) and 4(c), respectively. In both the ∥ and ⊥ components, a clear signature of oscillation is observed, suggesting towards the de Haas–van Alphen (dHvA) effect [57]. A strong magnetic anisotropy is observed between the ∥ and ⊥ components. At low H, the nonlinearity of the magnetization curves is observed. In the high-H regime, the diamagnetic component starts to dominate associated with the oscillation in the magnetization curve for the ∥ component, whereas it shows a paramagneticlike linear dependence along with the oscillation with the relatively smaller amplitude for the ⊥ component. The results indicate that the dHvA is dominant in the high-H regime and a nonlinear FM component is evident in the low H. After subtracting a smooth background, the oscillatory component exhibiting the maxima and minima in the ΔM versus $1/H$ curves is shown in Figs. 4(b) and 4(d) for the ∥ and ⊥ components, respectively. The amplitude of the oscillation at 140 kOe decreases rapidly with increasing T and disappears above ~25 and ~15 K for the ∥ and ⊥, respectively.

The Fast Fourier transform (FFT) of ΔM is depicted in the insets of Figs. 4(b) and 4(d). The FFT analysis provides a single temperature-independent frequency (F_{dHvA}) around 550 and 660 kOe for the ∥ and ⊥ components, respectively. The oscillation frequency correlates the extremal area of cross section (A_F) of the Fermi surface (FS), which is given by the Onsager relation $F_{\mathrm{dHvA}} = (\hbar/2\pi e)A_F$, with $A_F = \pi k_F^2$. Thus, the differences in F_{dHvA} point to an anisotropic FS, which is analogous to that observed for the parent Sb_2Te_3 [58]. The values of A_F and K_F are given in Table I for both the ∥ and ⊥ components. Temperature dependence

TABLE I. Parameters of the Fermi surface, as obtained from the analysis of the dHvA oscillation.

Component	F_{dHvA} (kOe)	A_F (10^{-3} Å^{-2})	K_F (10^{-2} Å^{-1})	m^* (m_0)	v_F (10^5 m/s)	T_D K	μ_q (10^3 cm^2 V^{-1} s^{-1})	l (nm)	τ 10^{-13} s
$\parallel$	550	5.4	4.2	0.23	2.1	10.7	0.87	23.5	1.1
$\perp$	660	6.4	4.5	0.25	2.1	3.9	2.1	66.8	3.1

of the amplitude of the oscillations, following the standard Lifshitz-Kosevich (LK) expression, can be expressed as $R_T = (2\pi^2 k_B T/\beta)/\sinh(2\pi^2 k_B T/\beta)$, where $\beta = e\hbar H/m^*$ [59,60]. Here, m^* is the effective cyclotron mass. The values of m^* are determined as $0.23m_0$ and $0.25m_0$ from the fit of the T dependence of the oscillation amplitude, as depicted in Figs. 5(a) and 5(b) for the $\parallel$ and $\perp$ component, respectively. Here, m_0 is the rest mass of a free electron. The value of m^* is significant, which is found to be massive compared to the pristine Sb_2Te_3 [61–63] and nonmagnetic element doped Sb_2Te_3 [64–66].

The H dependence of oscillation amplitude is verified further using LK formula $\Delta M = -H^{1/2} R_T \exp[-2\pi^2 k_B m^* T_D/\hbar eH]$ at 2 K [59,60] which are shown in Figs. 5(c) and 5(d) for both the $\parallel$ and $\perp$ component, respectively. Here, T_D is the Dingle temperature, which is obtained to be 10.7 and 3.9 K, respectively. Thus, the values of the quantum mobility $\mu_q = (e\hbar/2\pi k_B m^* T_D)$, the mean-free path ($l$), and lifetime $\tau = \hbar/(2\pi k_B T_D)$ of the charge carriers are further estimated, which are given in Table I. Although the $\perp$ component is comparable, the $\parallel$ component of μ_q is smaller than the classical Drude mobility, as obtained from the Hall measurement. This discrepancy may be attributed to the scattering, where the μ_q is sensitive to both the small- and large-angle scatterings. In contrast, the Drude mobility is influenced by the large-angle scattering [67]. The dHvA oscillation is explained by the Lifshitz-Onsager formula, considering the nth maxima to occur with $1/H$ using, $n + \gamma = \frac{\phi_0}{(2\pi\hbar)^2}(A_F/H)$, where γ is a phase and $\phi_0 = h/e$ [60]. Thus, the plot n with $1/H$ is linear following the Lifshitz-Onsagar formula. We calculate the Berry phase (γ) from the Landau-level fan diagram. The value of γ is crucial and it should be close to 0.5 for the Dirac particles and zero for the normal fermions [68,69]. The Landau-level fan diagrams are plotted from the dHvA oscillation, considering the maximum and minimum positions as integers and half-integers, respectively, which are shown in Figs. 5(e) and 5(f) for the $\parallel$ and $\perp$ components, respectively. The extrapolation of the plots at $1/H = 0$ meet at a particular point for both the components and provide the value of $\gamma = 0 \pm 0.01$. Thus, the fan diagram confirms that the Cr doping does not show the Dirac nature of the topological surface carriers, as established for the pristine Sb_2Te_3. Rather, a massive fermionic behavior with a parabolic nature of the dispersion curve is suggested having a surface exchange gap at the Dirac point. The possible nature of the gapped surface state is proposed in Fig. 5(g).

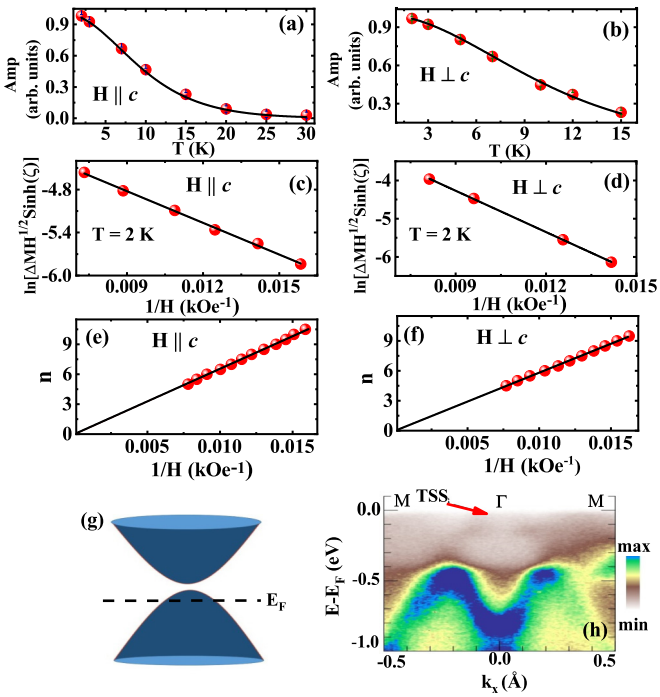

FIG. 5. Amplitude of the oscillatory component with temperature (T) for the (a) $\parallel$ and (b) $\perp$ components. The plot of $\ln[\Delta M H^{1/2}\sinh(\zeta)]$, where $\zeta = 2\pi^2 k_B m^* T_D/\hbar eH$, with $1/H$ for the (c) $\parallel$ and (d) $\perp$ components. The continuous curves are LK fit in (a)–(d). Landau-level fan diagram with the plot of n with $1/H$ for the (e) $\parallel$ and (f) $\perp$ components. (g) Schematic diagram of a gapped surface state with the possible Fermi energy level. (h) Experimental band structure along the $M\Gamma M$ symmetry direction at 70 K, as obtained from ARPES. Topological surface state (TSS) is indicated by an arrow.

The ARPES is a widely used and powerful experimental technique capable of mapping the occupied valence band structure of crystalline solid surfaces with high energy and wave-vector (k) resolution [70]. The valence band structure, as addressed by the ARPES, is depicted in Fig. 5(h). The topological surface state (TSS) is evident near the Fermi energy, as indicated by an arrow in the figure. Here, the band crosses the Fermi energy with the Dirac point located above it, in agreement with the reports for the pristine Sb_2Te_3 [71] as well as in the Cr-doped Sb_2Te_3 [72]. The result indicates that the Cr doping still keeps the material surface intrinsically p type. Here, the direct spectroscopic signature of the TRS breaking, attributed to the Cr magnetic moment, at the Dirac point is inaccessible from the ARPES study. At higher binding energy, an intense "M"-shaped band is visible which has been identified as a surface state in Sb_2Te_3 with Rashba spin splitting [73].

In order to understand possible magnetic order microscopically, we perform μSR measurements in zero field at low temperature. The zero-field (ZF) μSR measurements are carried out at different temperatures in the range of 2–40 K. The ZF asymmetry data at selected temperatures for $T \leqslant 10$ K are depicted in Fig. 6(a). At 2 K, a signature of a heavily damped oscillation, attributed to a magnetic order, is observed

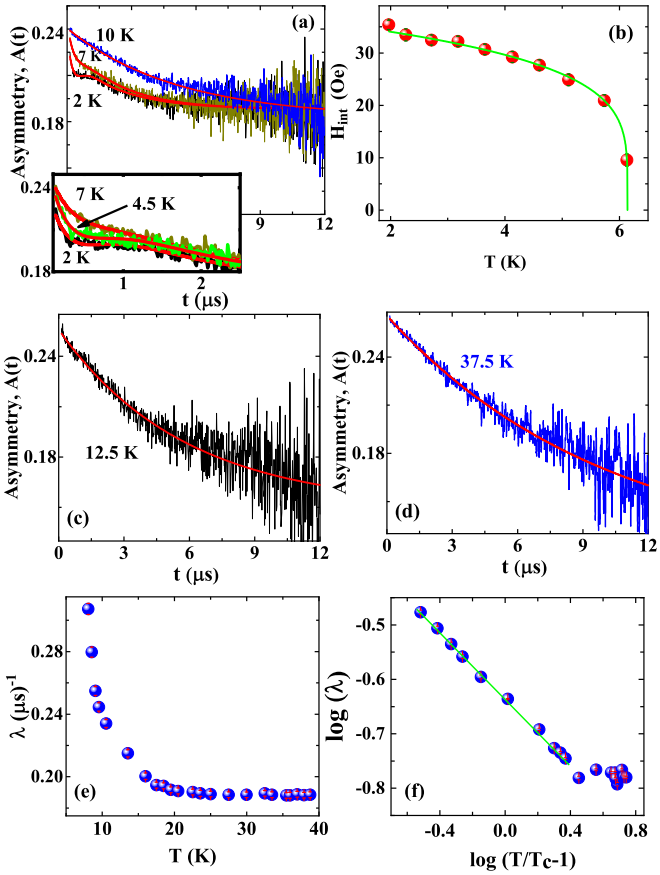

FIG. 6. Muon asymmetry data $A(t)$ with time (t) at selected temperature (T) in the range of (a) $2 \leqslant T \leqslant 10$ K, (c) 12.5 K, (d) 37.5 K. Inset of (a) amplifies the damped oscillation component further in the low-t region. (b) The internal magnetic field ($H_{\rm int}$) with T. The continuous curves show the fit. (e) Spin-lattice relaxation rate (λ) with T. (f) The log-log plot of λ versus $(T/T_C - 1)$. Straight line shows the fit, as described in the text.

below 1.5 μs in $A(t)$, which is further amplified in the inset of the figure. The oscillatory component rapidly decreases with increasing T and nearly vanishes close to 7 K. In case of heavily damped oscillation the muon asymmetry data have been modeled using the Kubo-Toyabe function, which is consistent with the static moment associated with the disordered electronic moments [74]. We note that the fit is not satisfactory with the Kubo-Toyabe function. The asymmetry $A(t)$ curve is further fitted with the following equation:

$$A(t) = A_{\rm base} + A_1 \cos(\gamma_\mu H_{\rm int} t + \phi) \exp(-\lambda_1 t) + A_2 \exp(-\lambda_2 t), \quad (3)$$

where $H_{\rm int}$ is the internal magnetic field corresponding to the magnetic order, ϕ is a phase factor, while λ's are the spin-lattice relaxation rates. Here, the base line, represented by $A_{\rm base}$, is found significantly high, which is attributed to the mounting of the crystals. The crystals with different size, shape, and thickness were mounted on the sample holder. Therefore, it would have been difficult to fix up the experimental condition, so that, all the muons would stop within the sample. The second and third terms in Eq. (3) express the muon spin precession and exponentially depolarized components with the initial asymmetries of A_1 and A_2, respectively. The second term is applied, when the muon spin precession exists. The satisfactory fit of the low-t muon decay at 2 K is shown in the inset of Fig. 6(a). The other fitted parameters are $A_{\rm base} = 0.163(6)$, $A_1 = 0.061(8)$, $A_2 = 0.067(4)$, $\lambda_1 = 0.46(0)$ $(\mu s)^{-1}$, $\lambda_2 = 0.294(0)$ $(\mu s)^{-1}$, $\phi = 1.14$, and $\chi^2 \sim 1.092$. The values of $H_{\rm int}(T)$, as obtained from the fit at low temperature, are shown in Fig. 6(b). With increasing T, the $H_{\rm int}$ decreases following $H_{\rm int}(T) = H_{\rm int}(0)[1 - T/T_C]^\beta$, where $H_{\rm int}(0)$ is the extrapolated internal magnetic field at 0 K, T_C is the magnetic ordering temperature, and β is a critical exponent [74–76]. The continuous curves in Fig. 6(b) provide the satisfactory fit with $H_{\rm int}(0) = 37.1(4)$ Oe, which are nearly one order of magnitude lower than the value for the insulating pyrochlore iridates [75] and spin-glasses [76]. However, the current value is nearly one order magnitude higher than the quasi-one-dimensional heavy-fermion system [74], as obtained from the μSR studies. Here, the value of β is close to that calculated value (0.23), reported for the 2D XY interaction [39,40].

Figures 6(c) and 6(d) exhibit the asymmetry curves above the magnetic order at 12.5 and 37.5 K, which are fitted to the first and last terms in Eq. (3), as shown by the continuous curves in the figures. The values of λ are depicted with T in Fig. 6(e). With decreasing T the $\lambda(T)$ exhibits a nearly T-independent behavior until ~22 K. The T-independent $\lambda(T)$ is often observed in a system with the localized moments, when the thermal fluctuation energy dominates over the exchange energy between the spins. Below ~22 K, the $\lambda(T)$ starts to increase slowly and a sharp increase of $\lambda(T)$ is observed with a further decrease in temperature, which appears due to the critical slowing down of the fluctuating moments while temperature approaches the magnetic order [77]. The slowing down of the critical fluctuations link to the divergence of spin-spin correlation as $\lambda(T) \propto [T/T_C - 1]^{-\omega}$, where ω is a dynamic exponent [78,79]. The linear log-log plot of λ against $[T/T_C - 1]$ is depicted in Fig. 6(f). The slope of the linear fit, using $T_C = 6.1$ K, provides $\omega = 0.30(6)$, proposing XY-type interaction [79].

A recent paper proposed that the nature of magnetic order was strongly influenced by the crystal structure and the surface electrons in case of magnetic-doped TI [5]. The first-principles calculations on the series of 3d transition metal (TM) dopants in Bi_2Te_3, Bi_2Se_3, and Sb_2Te_3 have been proposed that the structural difference associated with the role of surface electrons was found crucial for determining the magnetic structure [80]. Because of the low doping of TM in these series of chalcogenides, nature of the magnetic order has been rarely tested using any microscopic experiments. The spin dynamics and nature of magnetic interaction due to Mn doping in Bi_2Te_3 has been investigated using electron-spin resonance (ESR) technique, proposing a possible 2D character of the magnetic exchange interaction between the Mn dopants [81]. The 2D magnetic order was recently confirmed in $(Bi_{0.95}Mn_{0.05})_2Te_3$ using the neutron scattering techniques, where layered $R\bar{3}m$ structure has been correlated for the 2D magnetic order [10]. Analogous to that proposed in Bi_2Te_3 and Sb_2Te_3 having $R\bar{3}m$ structure, the Sb(Cr) atoms in $(Sb_{0.95}Cr_{0.05})_2Te_3$ occupy in a layered structure stacked along the c axis. We note that the intralayer nearest-neighboring

distance is 4.27 Å at 300 K, as obtained from our refined x-ray diffraction results. The distance between the quintuple layer is 6.16, whereas the distance within the quintuple layer is 4.70 Å along the c axis. Anticipating the same structure at low temperature, as suggested for the parent compound [82], the large interquintuple layer distance along the c axis may correlate the 2D character of the magnetic interaction. In the current investigation, trapping muon sites is very crucial, which leads to the character of the magnetic interactions.

The TIs have been originally proposed as the time-reversal invariant systems, where the onset of a spontaneous magnetization leads to the broken time-reversal symmetry and creates an exchange gap at the Dirac point [2,4]. In such magnetic TIs, tuning of the Fermi level in the exchange gap is one of the key parameters, which gives rise to an emergence of the quantum Hall effect at zero magnetic field. Magnetic doping turns out to be an efficient approach to break the TRS in 3D TIs to date. The current studies on the magnetic-doped TIs are still in a fledgling stage. Importantly, the nominal doping in TIs show a diversity in the electronic states, magnetic transition temperatures, anisotropies, and nature of the magnetic order even for the identical doping [2,4]. Thus, microscopic characterization of the magnetic properties of the doped materials needs to be carried out together with the comprehensive studies of the electronic states for the doped materials. In the current investigation, the heavily damped oscillations observed in the asymmetry curve below T_C further propose that the signal arises from the small magnetic phases, where the rest of the sample are magnetically disordered. However, these small magnetic phases are exchange coupled to account for a reasonable value of T_C. We note that this small static moment, attributed to the bulk 5% Cr doping in Sb_2Te_3, significantly influences the conducting surface electrons. The semimetallic conductivity of the dominant surface electrons associated with the improved magnetoresistance compared to the pristine compound is observed involving the reasonable Cr doping. The magnetization results clearly demonstrate the dHvA effect, which has been attributed to the surface effect. The Berry phase calculation, as estimated from the Landau-level fan diagram, proposes a gap at the Dirac point. The analysis of the μSR results suggests that a weak internal of $\sim$35 Oe close to 2 K is adequate for opening an exchange gap at the Dirac point. The analysis of the dHvA oscillation further designates that the effective mass significantly enhances compared to the pristine Sb_2Te_3, pointing that the charge carriers behave like a massive fermion. In the current observation, the Fermi level is proposed to be close to the top of the valence band, as indicated by an ARPES study. Tuning of the Fermi level within the exchange gap has been recognized as one of the promising studies in case of magnetic TIs, which might be involved with the possible occurrence of QAHE. The electron doping in $(Sb_{0.95}Cr_{0.05})_2Te_3$ may influence the shifting of the Fermi level towards the direction of the exchange gap, which has been considered as our future extended work.

In conclusion, the 5% Cr doping in Sb_2Te_3 integrates a magnetic order, which significantly influences the electronic structure at the surface. The μSR studies confirm a magnetic order with a T_C of $\sim$6.1 K. The heavily damped oscillations in the muon signal below T_C suggest the small static moments associated with the magnetically disordered background. The critical exponents indicate a 2D XY-type magnetic interaction. The magnetization curves exhibit the dHvA effect. Analysis of the dHvA effect infers that the charge carrier behaves like a massive fermion. The Berry phase suggests a possible opening of the surface state gap at the Dirac point.

ACKNOWLEDGMENTS

The authors would like to thank Dr. S. Banik for the valuable comments and discussions on the XPS and ARPES results. We would like to thank the Science and Technology Facility Council (STFC), Rutherford Appleton Laboratory (RAL), for allocation of the μSR beam time (RB2000035). T.K.D. wishes to acknowledge support from the DST-Inspire fellowship. The work of the groups in Hamburg and Kiel was funded by the Deutsche Forschungsgemeinschaft (DFG, German Research Foundation) – SFB-925 – project 170620586.

[1] M. Z. Hasan and C. L. Kane, Rev. Mod. Phys. **82**, 3045 (2010).
[2] Y. L. Chen, J.-H. Chu, J. G. Analytis, Z. K. Liu, K. Igarashi, H.-H. Kuo, X. L. Qi, S. K. Mo, R. G. Moore, D. H. Lu, M. Hashimoto, T. Sasagawa, S. C. Zhang, I. R. Fisher, Z. Hussain, and Z. X. Shen, Science **329**, 659 (2010).
[3] X. Kou, Y. Fan, M. Lang, P. Upadhyaya, and K. L. Wang, Solid State Commun. **215-216**, 34 (2015).
[4] Y. Tokura, K. Yasuda, and A. Tsukazaki, Nat. Rev. Phys. **1**, 126 (2019).
[5] R. S. K. Mong and J. E. Moore, Nature (London) **576**, 390 (2019).
[6] N. Nagaosa, J. Sinova, S. Onoda, A. H. MacDonald, and N. P. Ong, Rev. Mod. Phys. **82**, 1539 (2010).
[7] Q. L. He, L. Pan, A. L. Stern, E. C. Burks, X. Che, G. Yin, J. Wang, B. Lian, Q. Zhou, E. S. Choi, K. Murata, X. Kou, Z. Chen, T. Nie, Q. Shao, Y. Fan, S.-C. Zhang, K. Liu, J. Xia, and K. L. Wang, Science **357**, 294 (2017).
[8] N. H. Jo, K. J. Lee, C. M. Kim, K. Okamoto, A. Kimura, K. Miyamoto, T. Okuda, Y. K. Kim, Z. Lee, T. Onimaru, T. Takabatake, and M. H. Jung, Phys. Rev. B **87**, 201105(R) (2013).
[9] Y. S. Hor, P. Roushan, H. Beidenkopf, J. Seo, D. Qu, J. G. Checkelsky, L. A. Wray, D. Hsieh, Y. Xia, S.-Y. Xu, D. Qian, M. Z. Hasan, N. P. Ong, A. Yazdani, and R. J. Cava, Phys. Rev. B **81**, 195203 (2010).
[10] D. Vaknin, D. M. Pajerowski, D. L. Schlagel, K. W. Dennis, and R. J. McQueeney, Phys. Rev. B **99**, 220404(R) (2019).
[11] P. Sessi, F. Reis, T. Bathon, K. A. Kokh, O. E. Tereshchenko, and M. Bode, Nat. Commun. **5**, 5349 (2014).
[12] M. F. Islam, C. M. Canali, A. Pertsova, A. Balatsky, S. K. Mahatha, C. Carbone, A. Barla, K. A. Kokh, O. E. Tereshchenko, E. Jiménez, N. B. Brookes, P. Gargiani, M. Valvidares, S. Schatz, T. R. F. Peixoto, H. Bentmann, F. Reinert, J. Jung, T. Bathon, K. Fauth *et al.*, Phys. Rev. B **97**, 155429 (2018).

[13] S. Nakajima, J. Phys. Chem. Solids **24**, 479 (1963).
[14] H. J. Zhang, C. X. Liu, X. L. Qi, X. Dai, Z. Fang, and S. C. Zhang, Nat. Phys. **5**, 438 (2009).
[15] D. Kong, Y. Chen, J. J. Cha, Q. Zhang, J. G. Analytis, K. Lai, Z. Liu, S. S. Hong, K. J. Koski, S.-K. Mo, Z. Hussain, I. R. Fisher, Z.-X. Shen, and Y. Cui, Nat. Nanotechnol. **6**, 705 (2011).
[16] Y. Kim, A. DiVenere, G. K. L. Wong, J. B. Ketterson, S. Cho, and J. R. Meyer, J. Appl. Phys. **91**, 715 (2002).
[17] E. M. F. Vieira, J. Figueira, A. L. Pires, J. Grilo, M. F. Silva, A. M. Pereira, and L. M. Goncalves, J. Alloys Compd. **774**, 1102 (2019).
[18] W. Zhao, D. Cortie, L. Chen, Z. Li, Z. Yue, and X. Wang, Phys. Rev. B **99**, 165133 (2019).
[19] Z. Zhou, M. Žabèík, P. Lošták, and C. Uher, J. Appl. Phys. **99**, 043901 (2006).
[20] A. Singh, A. K. Ghosh, and S. Chatterjee, J. Supercond. Nov. Magn. **31**, 299 (2018).
[21] J. Horák, P. Lošt'ák, C. Drašar, J. S. Dyck, Z. Zhou, and C. Uher, J. Solid State Chem. **178**, 2907 (2005).
[22] H. Luo, Q. Gibson, J. Krizan, and R. J. Cava, J. Phys.: Condens. Matter **26**, 206002 (2014).
[23] W. Wang, C.-Z. Chang, J. S. Moodera, and W. Wu, npj Quantum Mater. **1**, 16023 (2016).
[24] Z. Zhou, Y.-J. Chien, and C. Uher, Appl. Phys. Lett. **87**, 112503 (2005).
[25] J. S. Dyck, T. J. Mitchell, A. J. Luciana, P. C. Quayle, Č. Drašar and P. Lošták, Appl. Phys. Lett. **91**, 122506 (2007).
[26] K. Sumida, M. Kakoki, J. Reimann, M. Nurmamat, S. Goto, Y. Takeda, Y. Saitoh, K. A. Kokh, O. E. Tereshchenko, J. Güdde, U. H. Öfer, and A. Kimura, New J. Phys. **21**, 093006 (2019).
[27] J. S. Dyck, P. Hájek, P. Lošták, and C. Uher, Phys. Rev. B **65**, 115212 (2002).
[28] J. Manson, A. Madubuonu, D. A. Crandles, C. Uher, and P. Lošták, Phys. Rev. B **90**, 205205 (2014).
[29] W. Zhang, D. West, S. H. Lee, Y. Qiu, C.-Z. Chang, J. S. Moodera, Y. S. Hor, S. Zhang, and W. Wu, Phys. Rev. B **98**, 115165 (2018).
[30] Y. Ruan, Y. Yang, Y. Zhou, L. Huang, G. Xu, K. Zhong, Z. Huang, and J.-M. Zhang, J. Phys.: Condens. Matter **31**, 385501 (2019).
[31] L. J. Collins-McIntyre, L. B. Duffy, A. Singh, N.-J. Steinke, C. J. Kinane, T. R. Charlton, A. Pushp, A. J. Kellock, S. S. P. Parkin, S. N. Holmes, C. H. W. Barnes, G. van der Laan, S. Langridge, and T. Hesjedal, Europhys. Lett. **115**, 27006 (2016).
[32] J. Horák, P. C. Quayle, J. S. Dyck, Č. Drašar, P. Lošták, and C. Uher, J. Appl. Phys. **103**, 013516 (2008).
[33] L. B. Duffy, A. I. Figueroa, L. Gladczuk, N.-J. Steinke, K. Kummer, G. van der Laan, and T. Hesjedal, Phys. Rev. B **95**, 224422 (2017).
[34] A. Singh, V. S. Kamboj, J. Liu, J. Llandro, L. B. Duffy, S. P. Senanayak, H. E. Beere, A. Ionescu, D. A. Ritchie, T. Hesjedal, and C. H. W. Barnes, Sci. Rep. **8**, 17024 (2018).
[35] Z. Zhou, Y.-J. Chien, and C. Uher, Phys. Rev. B **74**, 224418 (2006).
[36] J. S. Dyck, Č. Drašar, P. Lošták, and C. Uher, Phys. Rev. B **71**, 115214 (2005).
[37] V. A. Kulbachinskii, P. M. Tarasov, and E. Brück, Phys. B (Amsterdam) **368**, 32 (2005).
[38] F. Yang, Y. R. Song, H. Li, K. F. Zhang, X. Yao, C. Liu, D. Qian, C. L. Gao, and J.-F. Jia, Phys. Rev. Lett. **111**, 176802 (2013).
[39] S. T. Bramwell and P. C. W. Holdsworth, J. Phys.: Condens. Matter **5**, L53 (1993).
[40] S. T. Bramwell and P. C. W. Holdsworth, J. Appl. Phys. **73**, 6096 (1993).
[41] A. Taroni, S. Bramwell, and P. Holdsworth, J. Phys.: Condens. Matter **20**, 275233 (2008).
[42] http://dx.doi.org/10.5286/SOFTWARE/mantid.
[43] J. Gebhardt and A. M. Rappe, Phys. Rev. B **98**, 125202 (2018).
[44] T. K. Dalui, P. K. Ghose, S. Majumdar, and S. Giri, J. Phys.: Condens. Matter **32**, 435601 (2020).
[45] G. Zhang, H. Qin, J. Teng, J. Guo, Q. Guo, X. Dai, Z. Fang, and K. Wu, Appl. Phys. Lett. **95**, 053114 (2009).
[46] C. D. Wagner, J. Electron Spectrosc. Relat. Phenom. **32**, 99 (1983).
[47] Z. J. Yue, C. B. Zhu, S. X. Dou, and X. L. Wang, Phys. Rev. B **86**, 195120 (2012).
[48] V. A. Kulbachinskii, Z. M. Dashevskii, M. Inoue, M. Sasaki, H. Negishi, W. X. Gao, P. Lostak, J. Horak, and A. de Visser, Phys. Rev. B **52**, 10915 (1995).
[49] J. M. Ziman, in *Electrons and Phonons: The Theory of Transport Phenomena in Solids*, Classics Series (Oxford University Press, New York, 2001).
[50] R. H. McKenzie, J. S. Qualls, S. Y. Han, and J. S. Brooks, Phys. Rev. B **57**, 11854 (1998).
[51] Y. Kopelevich, J. C. Medina Pantoja, R. R. da Silva, and S. Moehlecke, Phys. Rev. B **73**, 165128 (2006).
[52] Y. L. Wang, L. R. Thoutam, Z. L. Xiao, J. Hu, S. Das, Z. Q. Mao, J. Wei, R. Divan, A. Luican-Mayer, G. W. Crabtree, and W. K. Kwok, Phys. Rev. B **92**, 180402(R) (2015).
[53] N. H. Jo, Y. Wu, L.-L. Wang, P. P. Orth, S. S. Downing, S. Manni, D. Mou, D. D. Johnson, A. Kaminski, S. L. Budko, and P. C. Canfield, Phys. Rev. B **96**, 165145 (2017).
[54] R. Singha, A. Pariari, B. Satpati, and P. Mandal, Phys. Rev. B **96**, 245138 (2017).
[55] X. Huang, L. Zhao, Y. Long, P. Wang, D. Chen, Z. Yang, H. Liang, M. Xue, H. Weng, Z. Fang, X. Dai, and G. Chen, Phys. Rev. X **5**, 031023 (2015).
[56] C. M. Hurd, *The Hall Effect in Metals and Alloys* (Plenum, New York, 1972).
[57] M. V. Kartsovnik, Chem. Rev. **104**, 5737 (2004).
[58] A. von Middendorff, K. Dietrich, and G. Landwehr, Solid State Commun. **13**, 443 (1973).
[59] Y. Ando, J. Phys. Soc. Jpn. **82**, 102001 (2013).
[60] D. Shoenberg, *Magnetic Oscillations in Metals* (Cambridge University Press, Cambridge, 1984).
[61] C. Weyrich, T. Merzenich, J. Kampmeier, I. E. Batov, G. Mussler, J. Schubert, D. Grüutzmacher, and Th. Schäpers, Appl. Phys. Lett. **110**, 092104 (2017).
[62] Y. Yan, E. Heintze, U. S. Pracht, M. Blankenhorn, and M. Dressel, Appl. Phys. Lett. **108**, 172407 (2016).
[63] L. Zhao, H. Deng, I. Korzhovska, M. Begliarbekov, Z. Chen, E. Andrade, E. Rosenthal, A. Pasupathy, V. Oganesyan, and L. Krusin-Elbaum, Nat. Commun. **6**, 8279 (2015).
[64] W. Zhao, L. Chen, Z. Yue, Z. Li, D. Cortie, M. Fuhrer, and X. Wang, npj Quantum Mater. **4**, 56 (2019).
[65] S.-M. Huang, Y.-J. Yan, S.-H. Yu, and M. Chou, Sci. Rep. **7**, 1896 (2017).
[66] V. A. Kulbachinskii, N. Miura, H. Nakagawa, H. Arimoto, T. Ikaida, P. Lostak, and C. Drasar, Phys. Rev. B **59**, 15733 (1999).

[67] A. Narayanan, M. D. Watson, S. F. Blake, N. Bruyant, L. Drigo, Y. L. Chen, D. Prabhakaran, B. Yan, C. Felser, T. Kong, P. C. Canfield, and A. I. Coldea, Phys. Rev. Lett. **114**, 117201 (2015).
[68] K. Shrestha, V. Marinova, D. Graf, B. Lorenz, and C. W. Chu, Phys. Rev. B **95**, 075102 (2017).
[69] K. Shrestha, D. E. Graf, V. Marinova, B. Lorenz, and P. C. W. Chu, Philos. Mag. **97**, 1740 (1997).
[70] S. Hüfner, *Photoelectron Spectroscopy* (Springer, Berlin, 1995).
[71] C. Seibel, H. Maaß, M. Ohtaka, S. Fiedler, C. Jünger, C.-H. Min, H. Bentmann, K. Sakamoto, and F. Reinert, Phys. Rev. B **86**, 161105(R) (2012).
[72] C.-Z. Chang, M.-H. Liu, Z.-C. Zhang, Y.-Y. Wang, K. He, and Q.-K. Xue, Sci. China-Phys. Mech. Astron. **59**, 637501 (2016).
[73] C. Pauly, G. Bihlmayer, M. Liebmann, M. Grob, A. Georgi, D. Subramaniam, M. R. Scholz, J. Sánchez-Barriga, A. Varykhalov, S. Blügel, O. Rader, and M. Morgenstern, Phys. Rev. B **86**, 235106 (2012).
[74] R. Sarkar, J. Spehling, P. Materne, H. Luetkens, C. Baines, M. Brando, C. Krellner, and H.-H. Klauss, Phys. Rev. B **95**, 121111(R) (2017).
[75] H. Guo, K. Matsuhira, I. Kawasaki, M. Wakeshima, Y. Hinatsu, I. Watanabe, and Z. A. Xu, Phys. Rev. B **88**, 060411(R) (2013).
[76] A. Shengelaya, G.-M. Zhao, C. M. Aegerter, K. Conder, I. M. Savić, and H. Keller, Phys. Rev. Lett. **83**, 5142 (1999).
[77] T. Moriya, Prog. Theor. Phys. **16**, 23 (1956).
[78] A. Berlie, I. Terry, and M. Szablewski, J. Mater. Chem. C **6**, 12468 (2018).
[79] F. Pratt, T. Lancaster, P. Baker, S. Blundell, W. Kaneko, M. Ohba, S. Kitagawa, S. Ohira-Kawamura, and S. Takagi, Phys. B (Amsterdam) **404**, 585 (2009).
[80] M. G. Vergniory, M. M. Otrokov, D. Thonig, M. Hoffmann, I. V. Maznichenko, M. Geilhufe, X. Zubizarreta, S. Ostanin, A. Marmodoro, J. Henk, W. Hergert, I. Mertig, E. V. Chulkov, and A. Ernst, Phys. Rev. B **89**, 165202 (2014).
[81] S. Zimmermann, F. Steckel, C. Hess, H. W. Ji, Y. S. Hor, R. J. Cava, B. Büchner, and V. Kataev, Phys. Rev. B **94**, 125205 (2016).
[82] A. N. Mansour, W. Wong-Ng, Q. Huang, W. Tang, A. Thompson, and J. Sharp, J. Appl. Phys. **116**, 083513 (2014).